

Quantitative Jones matrix imaging using vectorial Fourier ptychography

XIANG DAI,^{1,3} SHIQI XU,^{1,3} XI YANG,¹ KEVIN C. ZHOU,¹  CAROLYN GLASS,² PAVAN CHANDRA KONDA,¹  AND ROARKE HORSTMAYER^{1,*}

¹Department of Biomedical Engineering, Duke University, Durham, NC 27708, USA

²Department of Pathology, Duke University, Durham, NC 27708, USA

³These authors contributed equally

*roarke.w.horstmeyer@duke.edu

Abstract: This paper presents a microscopic imaging technique that uses variable-angle illumination to recover the complex polarimetric properties of a specimen at high resolution and over a large field-of-view. The approach extends Fourier ptychography, which is a synthetic aperture-based imaging approach to improve resolution with phaseless measurements, to additionally account for the vectorial nature of light. After images are acquired using a standard microscope outfitted with an LED illumination array and two polarizers, our vectorial Fourier ptychography (vFP) algorithm solves for the complex 2x2 Jones matrix of the anisotropic specimen of interest at each resolved spatial location. We introduce a new sequential Gauss-Newton-based solver that additionally jointly estimates and removes polarization-dependent imaging system aberrations. We demonstrate effective vFP performance by generating large-area (29 mm²), high-resolution (1.24 μ m full-pitch) reconstructions of sample absorption, phase, orientation, diattenuation, and retardance for a variety of calibration samples and biological specimens.

© 2022 Optica Publishing Group under the terms of the [Optica Open Access Publishing Agreement](#)

1. Introduction

Polarization imaging methods provide a useful means to access information about the molecular arrangement of anisotropic samples in a label-free manner [1], with applications spanning pathology [2–9], developmental biology [10], and mineralogy [11]. The retardance and diattenuation of the object can be at dimensions much smaller than the wavelength of light [12,13], revealing fine anisotropic structure in cells and materials. As such, polarization is an important and exciting intrinsic contrast mechanism in microscopy, especially in combination with phase contrast and fluorescence imaging approaches [14]. However, polarimetric imaging over wide areas at high resolution remains an outstanding challenge. Current microscopes that image at micrometer-level detail can observe a field-of-view (FOV) that covers several square millimeters [15], which makes polarimetric imaging of large specimens difficult.

Previously, Fourier ptychography (FP) was presented as a computational microscopy technique that allows imaging at simultaneously high resolution and wide fields of view (FOVs) (i.e., high space-bandwidth products (SBPs)) without moving parts [16]. However, FP traditionally only models light as a scalar field and thus ignores polarization information. While there has been some recent work in modeling polarization effects in FP [17], it only recovers a subset of the polarization information available. Here, we present vectorial FP (vFP) as a technique that models the vectorial nature of light, the sample, and the microscope itself to recover a more complete array of phase-sensitive polarimetric properties of the sample, including retardance, diattenuation, and orientation. Our work conceptually builds upon recent works in the related field of ptychography that have performed similar vectorial modeling for polarimetric imaging [18]. vFP thus avoids time-consuming step-and-repeat tiling strategies using expensive stages to create

large-area image composites [19], as well as minimizes the impact of polarization-dependent properties of the imaging system on the acquired measurements.

In the remainder of this paper, we will first review existing approaches for polarimetric imaging, then present the forward and inverse mathematical models for vectorial Fourier ptychography, before experimentally demonstrating its effective quantitative performance.

2. Background

There are three general categories of polarization-sensitive microscopic imaging. The first category captures qualitative polarimetric images, including placing a specimen between two polarizing films to visually assess relative variations in transmitted light [20,21] for diagnostic applications. To obtain quantitative polarimetric measurements, a second category of approach relies upon incoherent illumination to measure a specimen's Muller matrix [22], which describes the specimen's optical response via a 4×4 real-valued matrix at each spatial location of interest. In this class of intensity measurement-based methods, it is typical to describe light via a 4-entry Stokes vector, and a complete specimen reconstruction typically requires at least sixteen measurements per imaged pixel [23]. There have been a variety of optical geometries developed for full Mueller matrix-based polarization measurement [1,9,23–25]. By adopting circularly polarized specimen illumination and applying certain specimen approximations, various setups can obtain fewer image measurements to obtain specimen properties like birefringence and orientation [9].

A third category of quantitative polarimetric microscopy relies upon coherent light and can be described using the Jones Matrix formalism [26]. Within this category, the optical field is commonly modeled as two-dimensional complex vector, and associated optical transforms (including the interaction of light with thin specimens) as 2×2 complex matrix transforms. Typically, phase-sensitive measurements are needed to infer the 2×2 specimen Jones Matrix at each resolved location in the specimen. Prior work has considered this type of approach while detecting light with interferometry [27–34], optical coherence tomography [25,35], and laser scanning confocal microscopy [36], for example. Unlike incoherent techniques, phase-sensitive methods enable direct measurement of specimen phase retardance for topological information, as well as specimen diattenuation, which is the complex differential transmittance within independent polarization channels.

To alleviate the complexity introduced by interferometric detection methods, a number of strategies have been recently developed that jointly utilize a post-processing algorithm to assist with recovering a specimen's complex polarization-dependent properties [17,37–42]. These computational imaging-based techniques offer a variety of unique benefits, such as improved imaging speed and reduced system complexity. In this work, we achieve complex-valued Jones matrix imaging at high resolution over a large field-of-view by using principles FP [16]. Recent work has considered how FP can improve polarimetric imaging [17], but did not demonstrate the ability to recover the specimen's complex-valued Jones matrix, like many of the interferometric approaches above. Complex Jones matrix reconstruction offers a complete picture of the polarimetric properties of thin specimens and has been demonstrated in scanning-based ptychography [18,41], which uses a completely different measurement arrangement but is mathematically similar to FP [43,44]. In this work, we build upon these prior demonstrations in ptychography to jointly reconstruct quantitative, complex-valued Jones matrix measurements at high-resolution over a large area, along with the additional benefit of computationally accounting for polarization-dependent imaging system aberrations. The key benefits of our vFP approach are thus 1) the ability to reconstruct the complex Jones matrix of a specimen, from which we are able to derive phase, amplitude, retardance, slow-axis orientation, and diattenuation, 2) the ability to do so at a spatial resolution that surpasses the standard optical limit defined by the imaging lens,

and 3) the ability to jointly remove the effects of polarization dependent aberrations from final high space-bandwidth product image reconstructions.

3. Methods

3.1. vFP forward model

We begin by developing a mathematical expression for Fourier ptychographic imaging using Jones calculus, which will allow us to describe our data collection strategy using vectorial optical fields. A diagram of the vFP optical setup is in Fig. 1(a). To begin, we restrict our analysis to optically thin specimens that obey the projection approximation. This limits our attention in this work to polarization-dependent effects along x and y , although future work may extend analysis to examine thicker specimens and effects along z . A complete derivation of our forward

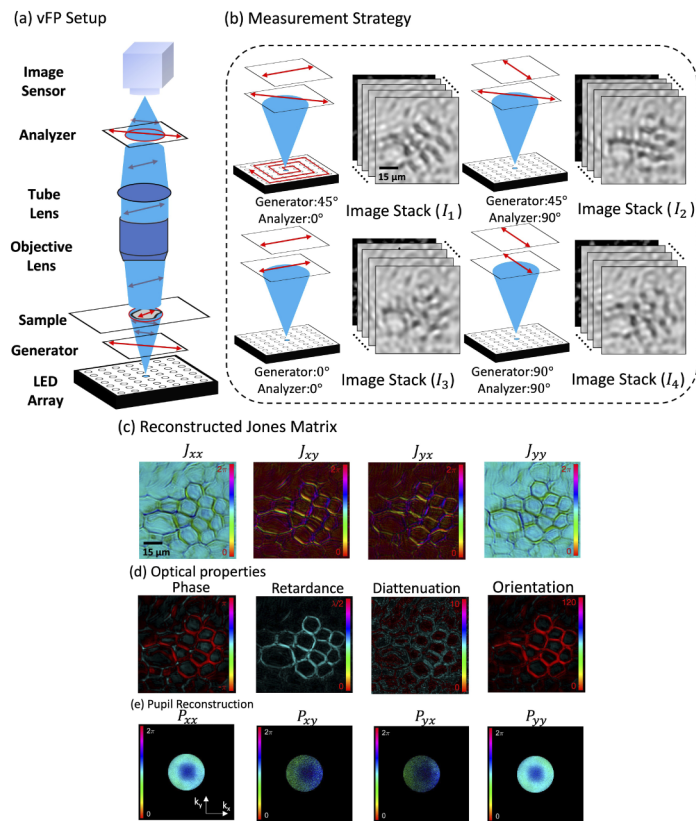


Fig. 1. Overview of vectorial Fourier ptychography (vFP). (a) vFP optical setup consists of a standard polarized light microscope modified with an LED array source to sequentially illuminate specimens with light polarized by generator. Light scattered in polarization-dependent manner passes through an analyzer before being recorded by the image sensor. (b) Images are acquired for each LED under four different generator-analyzer configurations under red light illumination (632 nm center wavelength). (c) 4-channel Jones Matrix vFP reconstruction of the cross-section of a broad bean root (color shows phase, and the saturation denotes amplitude, which is normalized between 0 and 1). (d) Various polarization-dependent sample properties extracted from the Jones matrix using eigenvector analysis. (e) vFP simultaneously measures a polarization-dependent pupil function as it removes associated per-channel aberrations.

model, beginning from Maxwell's equations in 3D, is presented in Supplementary Section 1. Our forward model is based on paraxial approximation, which has been validated to be accurate for up to 25 degree illumination angle in a previous work [30]. Jones calculus represents an optical field as a 2×1 complex vector containing two orthogonal components, which we define here along the x and y axes. The light's polarization state is defined by the amplitude and phase of these two components at each spatial location of interest. General optical transformations (e.g., passage through an optical component) are summarized by 2×2 complex matrices. We note that the Jones calculus employed here does not directly consider depolarizing effects, or 3D effects, for example, which can easily be added in at the expense of a more complex model.

Our setup consists of a programmable LED array as illumination source, a generator polarizer placed between the sample and the LED array, standard microscope optics, a CMOS camera, and an analyzer polarizer placed between the optics and camera. The n th tilted plane wave emitted by the n th LED within the array is described by $\exp(i\mathbf{k}_n \cdot \mathbf{r})$, which is polarized by the generator to form a 2×1 vector field, $\mathbf{G}_n^m = [g_x^m \exp(i\mathbf{k}_n \cdot \mathbf{r}), g_y^m \exp(i\mathbf{k}_n \cdot \mathbf{r})]^T$, which is obliquely-incident on the sample of interest. Here, $m \in \{0^\circ, 45^\circ, \dots\}$ specifies a particular polarization state, and we use $\mathbf{g}_m = [g_x^m, g_y^m]$ as complex-valued scalars to define the appropriate generator-dependent weighting for each vector component. The polarized plane wave \mathbf{G}_n^m then interacts with the thin specimen of interest, which we model as a product with a 2×2 complex matrix $\bar{\mathbf{O}}(\mathbf{r})$.

The resulting field then propagates to the imaging system's back focal plane, which we model (under certain approximations) with a 2×2 matrix \mathbf{F} that contains the two dimensional Fourier transform operator \mathcal{F} along its diagonal. Scalar FP models imaging system aberrations with a scalar pupil function $P(k)$ [45]. In this work, we extend this model to also allow for polarization-dependent aberrations with a 2×2 complex pupil function matrix $\mathbf{P}(\mathbf{k})$. This matrix can accounts for both standard aberrations (e.g., defocus, astigmatism), and for more complex polarization-dependent effects, for example birefringence introduced by plastic lenses, or polarization-dependent effects that occur at high angles of light incidence at general interfaces.

After passage through the pupil function (i.e., multiplication with $\mathbf{P}(\mathbf{k})$), the vectorized field then propagates to the image plane, which we model here with a 2×2 (inverse) Fourier transform matrix, although alternative transforms can be directly inserted. The vector field finally passes through a second "analyzer" polarizer, \mathbf{A}_l , ($l \in \{0^\circ, 45^\circ, \text{right circular}, \dots\}$), to produce the n th vector field $\mathbf{E}_n^{(l,m)}$ at the image plane,

$$\mathbf{E}_n^{(l,m)} = \mathbf{A}_l \mathbf{F}^{-1} \mathbf{P}(\mathbf{k}) \bar{\mathbf{O}}(\mathbf{r}) \mathbf{G}_n^m \quad (1)$$

where

$$\bar{\mathbf{O}}(\mathbf{r}) = \begin{bmatrix} \bar{O}_{xx}(\mathbf{r}) & \bar{O}_{xy}(\mathbf{r}) \\ \bar{O}_{yx}(\mathbf{r}) & \bar{O}_{yy}(\mathbf{r}) \end{bmatrix}, \mathbf{P}(\mathbf{k}) = \begin{bmatrix} P_{xx}(\mathbf{k}) & P_{xy}(\mathbf{k}) \\ P_{yx}(\mathbf{k}) & P_{yy}(\mathbf{k}) \end{bmatrix} \quad (2)$$

are the Jones matrices of the spectrum of the sample and pupil. We can take advantage of the Fourier shift theorem to remove the first Fourier transform matrix, and instead describe a shifted sample spectrum across the pupil plane, caused by each plane wave traveling at angle \mathbf{k}_n , as $\mathbf{O}(\mathbf{k} - \mathbf{k}_n)$, where \mathbf{O} is the Fourier transform of $\bar{\mathbf{O}}$. This leads to the following compact form of the vFP forward model for each detected intensity image i under illumination from the n th LED angle with generator and analyzer configurations (l, m):

$$i_n^{l,m}(\mathbf{O}, \mathbf{P}) = |\mathbf{a}_l^T \mathbf{F}^{-1} \mathbf{P}(\mathbf{k}) \mathbf{O}(\mathbf{k} - \mathbf{k}_n) \mathbf{g}_m|^2, \quad (3)$$

where \mathbf{a}_l and \mathbf{g}_m is the Jones vector of the l^{th} analyzer and g^{th} generator, respectively. In our first demonstration we use linear polarizers for both generator and analyzer, as will be discussed in the next subsection, we have $\mathbf{a}_l = [\cos \alpha_l, \sin \alpha_l]^T$, and $\mathbf{g}_m = [\cos \gamma_m, \sin \gamma_m]^T$, where α_l and γ_m are the angles of the linear polarizers of the l^{th} analyzer and g^{th} generator, respectively. The

goal of vFP is to jointly recover the complex 2×2 matrices describing the specimen and pupil function, \mathbf{O} and \mathbf{P} , from an acquired image dataset $i_n^{l,m}$ for multiple illumination angles $n = 1$ to N and multiple configurations of the generator l and the analyzer m . There are various possible selections for these measurement variables, and we next describe one effective measurement strategy that yields a well-conditioned image dataset for inverse problem estimation.

3.2. Measurement strategy

Obtaining four unique measurements per illumination angle is one effective strategy to solve for the four unknowns summarized by the sample matrix $\mathbf{O}(\mathbf{k})$. There are, of course, many possible configurations of the generator and analyzer to utilize for such measurements [18]. Specific selections significantly reduce the complexity of Eq. (3). For example, selecting the generator (G) and the analyzer (A) to produce and admit zero-degree linearly polarized light will result in $\mathbf{g}_m = [1, 0]^T$ and $\mathbf{a}_l = [1, 0]^T$. The resulting image intensity will be described by $i_n^{l=0^\circ, m=0^\circ} = |\mathcal{F}^{-1}[P_{xx}O_{xx}(\mathbf{k} - \mathbf{k}_n) + P_{xy}O_{yx}(\mathbf{k} - \mathbf{k}_n)]|^2$ for plane wave illumination at an angle \mathbf{k}_n . Setting the generator and the analyzer at 90 degrees will likewise yield additional complementary information about \mathbf{O} and \mathbf{P} . The above two configurations provide the helpful benefit of high optical transmission for most specimens of interest, which facilitates the use of lower exposure times and reduced noise. To balance the experimental benefits of high optical transmission with the computational benefits of measurement redundancy, we next set the generator (G) at 45° for our remaining two measurements. Our four polarization configurations were thus, $(l, m) \in \{G: 0^\circ, A: 0^\circ; G: 90^\circ, A: 90^\circ; G: 45^\circ, A: 0^\circ; G: 45^\circ, A: 90^\circ\}$, as shown in Fig. 1. We note that alternative generator/analyzer configurations are certainly possible and compatible with our forward and inverse solver, and will be the subject of future study.

3.3. Inverse problem

Using the measurement strategy proposed in Section 3.2, the four amplitude measurements for the n^{th} LED are

$$\begin{cases} i_n^{0^\circ, 0^\circ}(\mathbf{r}) = |\mathcal{F}^{-1}\{P_{xx}(\mathbf{k}) \cdot O_{xx}(\mathbf{k} - \mathbf{k}_n) + P_{xy}(\mathbf{k}) \cdot O_{yx}(\mathbf{k} - \mathbf{k}_n)\}|^2 & (4a) \\ i_n^{90^\circ, 90^\circ}(\mathbf{r}) = |\mathcal{F}^{-1}\{P_{yy}(\mathbf{k}) \cdot O_{yy}(\mathbf{k} - \mathbf{k}_n) + P_{yx}(\mathbf{k}) \cdot O_{xy}(\mathbf{k} - \mathbf{k}_n)\}|^2 & (4b) \\ i_n^{45^\circ, 0^\circ}(\mathbf{r}) = |\mathcal{F}^{-1}\{P_{xx}(\mathbf{k}) \cdot O_{xx}(\mathbf{k} - \mathbf{k}_n) + P_{xy}(\mathbf{k}) \cdot O_{yx}(\mathbf{k} - \mathbf{k}_n) \\ \quad + P_{xy}(\mathbf{k}) \cdot O_{yx}(\mathbf{k} - \mathbf{k}_n) + P_{xy}(\mathbf{k}) \cdot O_{yy}(\mathbf{k} - \mathbf{k}_n)\}|^2 & (4c) \\ i_n^{45^\circ, 90^\circ}(\mathbf{r}) = |\mathcal{F}^{-1}\{P_{yy}(\mathbf{k}) \cdot O_{xx}(\mathbf{k} - \mathbf{k}_n) + P_{yx}(\mathbf{k}) \cdot O_{xy}(\mathbf{k} - \mathbf{k}_n) \\ \quad + P_{yy}(\mathbf{k}) \cdot O_{yx}(\mathbf{k} - \mathbf{k}_n) + P_{yy}(\mathbf{k}) \cdot O_{yy}(\mathbf{k} - \mathbf{k}_n)\}|^2. & (4d) \end{cases}$$

We have developed an iterative algorithm to estimate the complex-valued object and pupil matrices (extending scalar phase recovery [46,47] to the vector case) by minimizing the Euclidean distance between predicted and measured amplitude,

$$\mathcal{D}(\mathbf{O}, \mathbf{P}) = \frac{1}{2N} \sum_n \sum_{(l,m)} \left\| \sqrt{i_n^{l,m}(\mathbf{O}, \mathbf{P})} - \sqrt{\hat{i}_n^{l,m}(\mathbf{r})} \right\|_2^2. \quad (5)$$

Here, N is the total number of illumination angles, while $i_n^{l,m}(\mathbf{O}, \mathbf{P})$ and $\hat{i}_n^{l,m}$ are the vFP forward model prediction (Eq. (4)) and the actual experimental image measurements for the n^{th} LED illumination using the (l, m) th generator-analyzer configuration. To minimize the loss function $\mathcal{D}(\mathbf{O}, \mathbf{P})$, we use a Gauss-Newton-based sequential solver, which alternatively updates the object and pupil matrix estimations based upon the 4 polarization measurements from each

LED. Our method is inspired by prior ptychographic phase retrieval solvers like the sequential Gauss-Newton (GN) method [46] and regularized ptychographic iterative engine (rPIE) [47], which use CR-calculus [48] to estimate the gradient of the loss with respect to both sample and pupil. In our approach, we stack 4 image measurements into a per-LED measurement vector and also compute a complex-valued loss function gradient. Unlike prior work, minimizing the loss function with a GN method requires inversion of a non-diagonal system matrix due to mixing of polarization states. This adds several complexities as compared to matching computations with scalar fields, which can effectively use a direct division for inversion [46,47]. We refer the interested reader to a complete presentation and derivation of our algorithm in the Supplementary Material.

Once we reconstruct the 2×2 Jones matrix for the specimen and pupil, we use a simple eigen decomposition method [1] to derive the homogeneous anisotropic properties of the specimen, including retardance, diattenuation and orientation. Specifically, for the 2×2 Jones matrix $\tilde{\mathbf{O}}(\mathbf{r})$ per reconstructed pixel, we first compute eigenvalues ξ_q, ξ_r and eigenvectors $\mathbf{E}_q, \mathbf{E}_r$. Under the assumption of homogeneous anisotropic specimen, the calculated eigenvectors indicate two perpendicular specimen axes with associated eigenvalues that can be used to compute a per-pixel retardance,

$$B = \frac{\lambda}{2\pi} |\angle \xi_q - \angle \xi_r|, \quad (6)$$

where \angle denotes complex angle. Similarly, the two eigenvalues may be used to compute an amplitude-dependent diattenuation measurement:

$$D = \left| \frac{|\xi_q|^2 - |\xi_r|^2}{|\xi_q|^2 + |\xi_r|^2} \right|. \quad (7)$$

In this work, we adopt a definition for orientation as the angle between the reference axis given by the linear polarizer within the setup and the slow axis within the specimen plane, where the slow axis is defined by the direction of the eigenvector whose corresponding eigenvalue phase is the larger of ξ_q and ξ_r . Mathematically, orientation to the slow axis ω can be computed as the angle of the eigenvector,

$$\omega = \tan^{-1}(E_{i,x}/E_{i,y}), \quad i = \arg \max_{i \in \{q,r\}} \angle \xi_i, \quad (8)$$

where $E_{\cdot,x}$ and $E_{\cdot,y}$ are the real x and y components of the eigenvector, respectively.

4. Results

We verified our vFP model and inverse solver in a series of experiments using a standard microscope outfitted with an LED array. The vFP setup uses an objective lens ($4\times$, $NA_o=0.1$) and digital camera containing $2.4 \mu\text{m}$ pixels (Basler acA5472-17um, 5496×3672 pixel count). The LED array (Adafruit RGB LED Matrix) contains 15×15 surface-mounted elements (center wavelengths: 632 nm, 525 nm and 470 nm per LED color with 4 mm LED pitch). We positioned the LED array 68 mm beneath the sample to create a maximum illumination NA of $NA_i = 0.41$. This leads to an effective synthetic NA for our Fourier ptychographic reconstructions of $NA = NA_i + NA_o = 0.51$, or a 5x improvement in spatial resolution in each lateral dimension. Linear wire grid polarizers (polarization wavelength range between 420 - 700 nm) were inserted directly before the LED array (generator) and before the camera (analyzer). Both linear polarizers were installed in rotation mounts (Thorlabs ELL14K) with resonant piezoelectric motors (bidirectional accuracy, 0.002°). The total data acquisition for 81 images (81 different LED positions) for each polarization configuration is around 50 seconds. The total reconstruction time is around 200 seconds for a 300 μm by 300 μm field of view.

4.1. Validation of vFP resolution and diattenuation

To first validate that the polarization-dependent metrics of vFP exhibit the expected resolution enhancement commonly observed with scalar FP, we imaged a sample consisting of a plastic linear polarizer (Edmund Optics) placed above a high-resolution absorptive USAF target (Ready Optics). The linear polarizer provides a simple means to create an expected constant orientation and a uniform diattenuation across the regions it covers, while the USAF target provides a standard resolution measure.

The expected resolution gain of a vFP reconstruction follows the same principles as with scalar FP [49], wherein the smallest resolvable full-pitch resolution (i.e., distance between the center of two similar bars) can be approximated by, $\frac{\lambda}{NA_i + NA_o}$. Using red LED illumination (center wavelength 632 nm) in this experiment, we accordingly expect a 1.24 μm full-pitch resolution cutoff after executing vFP, which corresponds to a cutoff slightly above USAF target Group 9 Element 5. The vFP orientation reconstruction achieves this resolution as shown in Fig. 2(d), which provides an appreciable gain over the raw captured image intensity in (c).

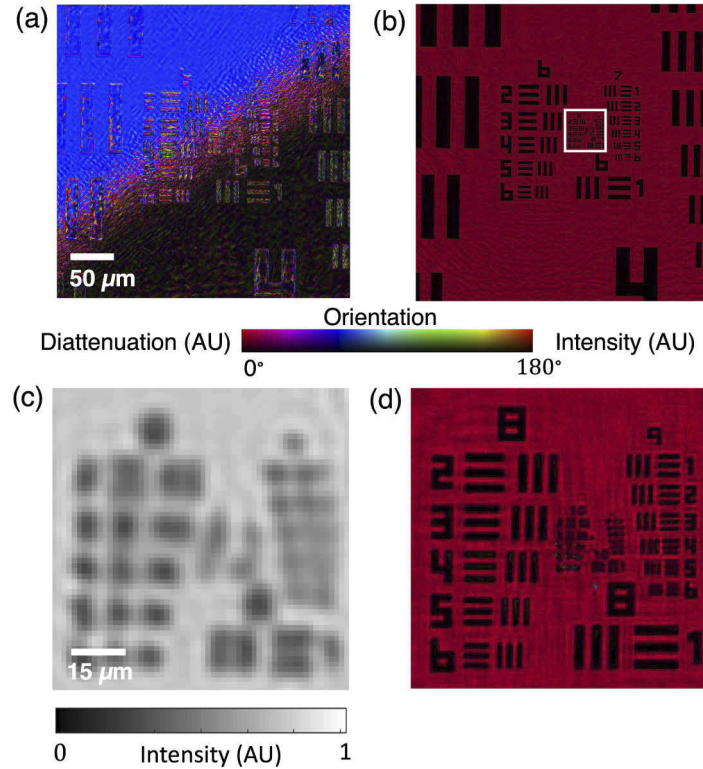


Fig. 2. Verification of vFP diattenuation estimation accuracy, as well as resolution gain, using a resolution target and linear polarizer (carried out at 632 nm). (a) Diattenuation (brightness) and orientation (hue) of vFP reconstruction with USAF target half covered (in the upper left) by a linear polarizer. (b) Incoherent sum of squared channel amplitudes (displayed as variations in brightness) and orientation (displayed as variations in hue) of USAF target fully covered by the linear polarizer, rotated by 48 degrees as compared to placement in (a). (c) Zoom-in of the raw intensity image (shown in grayscale) captured under illumination from center LED. (d) Zoom-in of the vFP reconstruction in (b) verifies resolution gain, using the same brightness/hue representation of the reconstructed scalar sum/orientation as in (b).

This linear polarizer experiment additionally provides a means to assess quantitative diattenuation and orientation measurement accuracy. As only the upper-left of the USAF target is covered by the polarizer in Fig. 2(a), we expect a diattenuation value closer to 1 within this region, and close to 0 in the lower right, which is uncovered. The mean diattenuation and variance, averaged across a 500^2 pixel area within these two respective regions, are ($\bar{D} = 0.9822, \sigma_D^2 = 0.001$) and ($\bar{D} = 0.0693, \sigma_D^2 = 0.011$), respectively. We hypothesize that this experimentally measured diattenuation of less than 1 is due to the use of a plastic linear polarizer as the investigated specimen, which did not completely polarize all transmitted light. This effect leads to slight deviations in measured image intensity values as compared to expectations for a perfect linear polarizer, which impacts the subsequent computation of diattenuation via Eq. (7). In addition, the transition boundary between the image area covered and uncovered by linear polarizer exhibits inaccurate values due to angle-dependent shadowing effects introduced by its finite thickness (i.e., the polarizer does not obey the required thin specimen approximation, leading to such artifacts). The diattenuation estimates at locations of absorptive USAF bars may also be inaccurate, as the bars are optically opaque.

4.2. Quantitative orientation measurement

Orientation is a useful polarimetric quantity used within material and biological specimen analysis. To further investigate the quantitative accuracy of vFP for specimen orientation measurement, we next imaged a collection of randomly-oriented monosodium urate (MSU) crystals, which are rod-like microstructures whose optical orientation properties are expected to exhibit a linear relationship with crystal rotation angle within the x-y plane. A summary of this experiment's results is presented in Fig. 3(a). Images of 3 example reconstructed MSU crystals are included as insets (color denotes reconstructed orientation and intensity denotes reconstructed retardance). Plotting the vFP-measured per-crystal orientation versus the expected orientation, as measured from crystal rotation angle within the x-y plane, reveals a clear linear relationship. Measured orientation points were averaged over all pixels within each crystal, where the error bar shows the resulting standard deviation. Ground-truth orientations were computed by fitting a line to each MSU crystal captured within a single FOV.

In a final experiment to assess vFP's ability to measure orientation, we imaged a thin section of human connective tissue containing both muscle and collagen (Fig. 3(b-c)). In this type of tissue specimen, it is common to observe polarization-dependent effects due in part to the response of collagen fiber [50,51]. To improve visualization, we overlay orientation as an undirected vector field on top of the retardance shown in grayscale in Fig. 3(c) to reveal a spatial correlation between retardance and orientation. Reconstructed orientation vector alignment is consistent with fiber growth direction within the connective tissue. We note the FOV in (c1) matches that of the example raw image is shown in (b2) and the zoom of the vFP reconstruction in (b3).

4.3. Retardance and phase validation

To validate that vFP can accurately measure retardance and phase, we imaged microspheres embedded in several media with different refractive indices (RIs). Here, microspheres are versatile validation samples not only because they have been commonly used to validate the quantitativity of phase estimation in conventional FP (e.g., [52]), but also because recent work has established a linear relationship between retardance and RI difference at the microsphere boundaries [42]. Though microspheres do not intrinsically exhibit birefringence, a sharp RI transition at their boundary will lead to a measurable retardance shift that is linearly proportional to the RI difference at the transition boundary [53]. To explore this connection, we prepared 3 specimens of oil-immersed polystyrene microspheres with oils of 3 different RI to generate 3 unique RI transition differences. Images of vFP-reconstructed retardance are in Fig. 4(a) top, from which we observe a clear peak of retardance that consistently exists at the bead profile edge

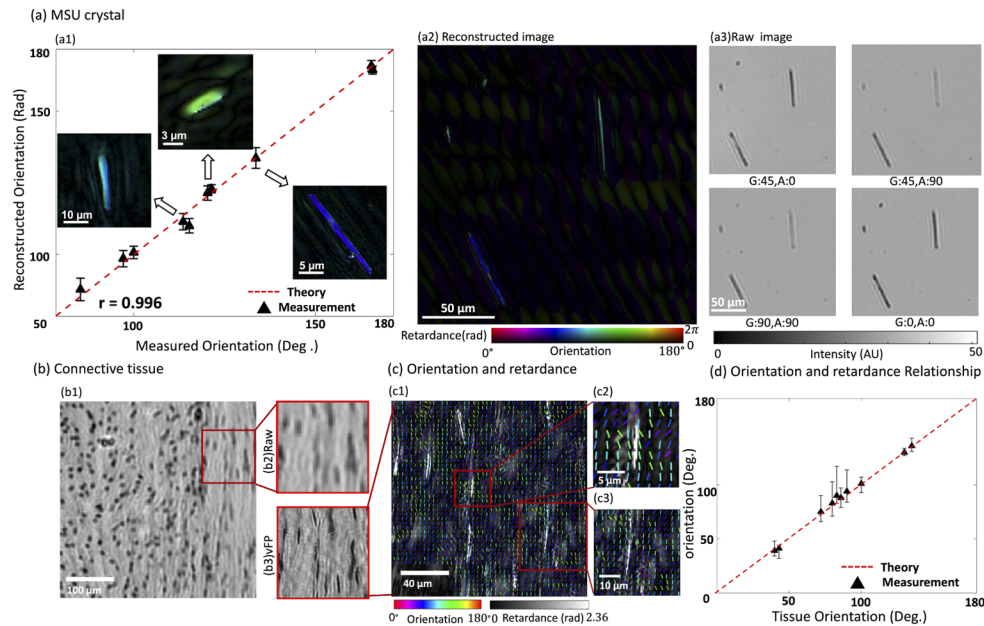


Fig. 3. Orientation measurement validation, carried out at a center wavelength of 525 nm. (a1-a2) vFP orientation reconstruction of monosodium urate (MSU) crystals (y-axis) exhibit expected linear relationship with crystal rotation angle (x-axis). (a1) Each point reports average and standard deviation (error bar) of per-crystal vFP orientation measurement averaged over pixels within each crystal (examples in 3 insets, color is orientation and intensity is retardance). (a2) shows a reconstructed image containing several sparsely distributed MSU. (b) Raw image and vFP reconstruction of human connective tissue specimen. (b1) Example raw image and (b2) zoom-in. (b3) vFP reconstruction shown as incoherent summation of matrix elements. (c) vFP retardance and orientation of the same area as in (b2-3), where (c1) shows retardance in grayscale intensity and orientation false-colored and (c2, c3) are zoom-in of regions highlight how specimen orientation follows fiber growth direction. (d) plots the orientations of tissue retardance vs reconstructed slow axis orientation, suggesting the two features are correlated.

(i.e., forms a ring around each bead). Profiles of randomly selected beads below confirm such peak formation, from which we measure the maximum per-bead retardance shift (red dashed line). Plotting the average maximum retardance shift (20 beads per point) as a function of RI difference in Fig. 4(b) confirms the previously observed linear trend. Through this experimental analysis, we were additionally able to confirm the quantitative accuracy of vFP reconstructed phase values, as shown at the bottom of Fig. 4(a) and summarized in plot of average maximum phase shift versus RI difference in Fig. 4(c).

4.4. Large-area amyloid plaque detection

We next applied vFP to reconstruct the vectorial response of a specimen that is commonly viewed using polarization optics within the pathology lab: thin sections of fixed cardiac tissue stained with Congo red dye. Congo red is known to stain specimen areas that contain amyloid fibrils an 'apple-green' color when viewed between two crossed polarizers using white light illumination in a transmission geometry, resulting from an interplay between birefringence and anomalous dispersion around an absorption peak [20]. Visual identification of such apple-green areas within the interstium and vessel walls of endomyocardial tissue is often an important diagnostic indicator

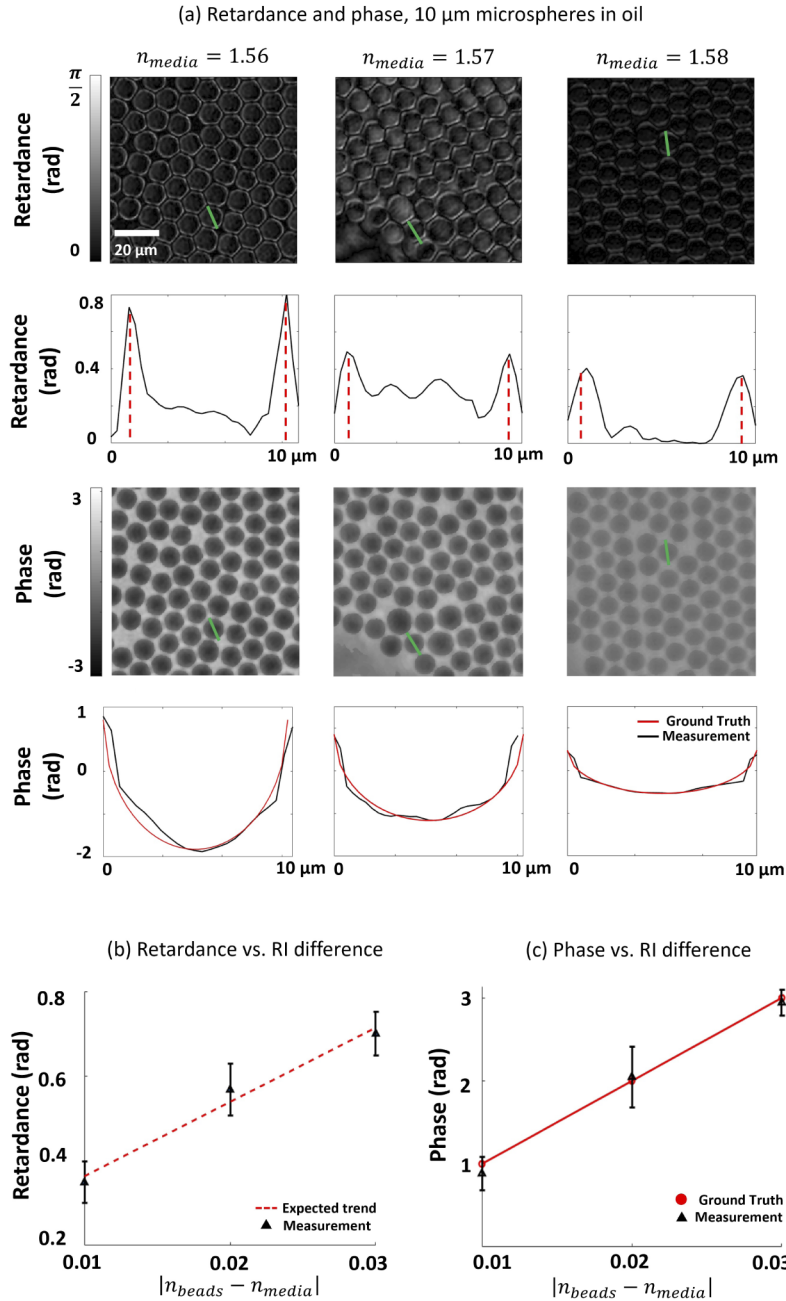


Fig. 4. vFP retardance and phase validation experiments (carried out at 525 nm). (a) Retardance (top two rows) and phase (bottom two rows) reconstructions of 10- μm monodisperse polystyrene microspheres immersed in oils with refractive indices (RIs) of 1.56, 1.57 and 1.58. Profiles through select beads show RI-dependent retardance shift at bead-oil boundary measured with red-dotted line, while phase profiles closely match ground truth shift. (b) Reconstructed maximum retardance shift (red dashed line in (a), average of 20 beads per point) follows expected linear trend with RI difference between microspheres and oil. (c) Reconstructed max. phase shift also follows ground truth (average of 20 beads per point).

of the presence of cardiac amyloidosis. In Fig. 5(a,b), we present a large-FOV vFP reconstruction (8.27 mm^2 shown) of the phase and retardance of Congo red-stained cardiac tissue, wherein the arterial wall is clearly visible. Interestingly, in Fig. 5(f), the red blood cells (small, dark circular features) located within the vessels each exhibit a higher retardance along their border, which is consistent with our observations with polystyrene beads (Fig. 4). Examining the difference between the red and green channels simulated using reconstructed Jones matrices highlights the amyloid plaque regions in Fig. 5(g). Comparing the resulting channel difference map to what is typically observed with polarization optics in a standard microscope (white-light illumination, NA=0.25) demonstrates a close qualitative correspondence (Fig. 5(h)). We hypothesize that vFP can thus provide a useful tool for examining the polarimetric response of such Congo-red-stained cardiac tissue over large areas at high resolution.

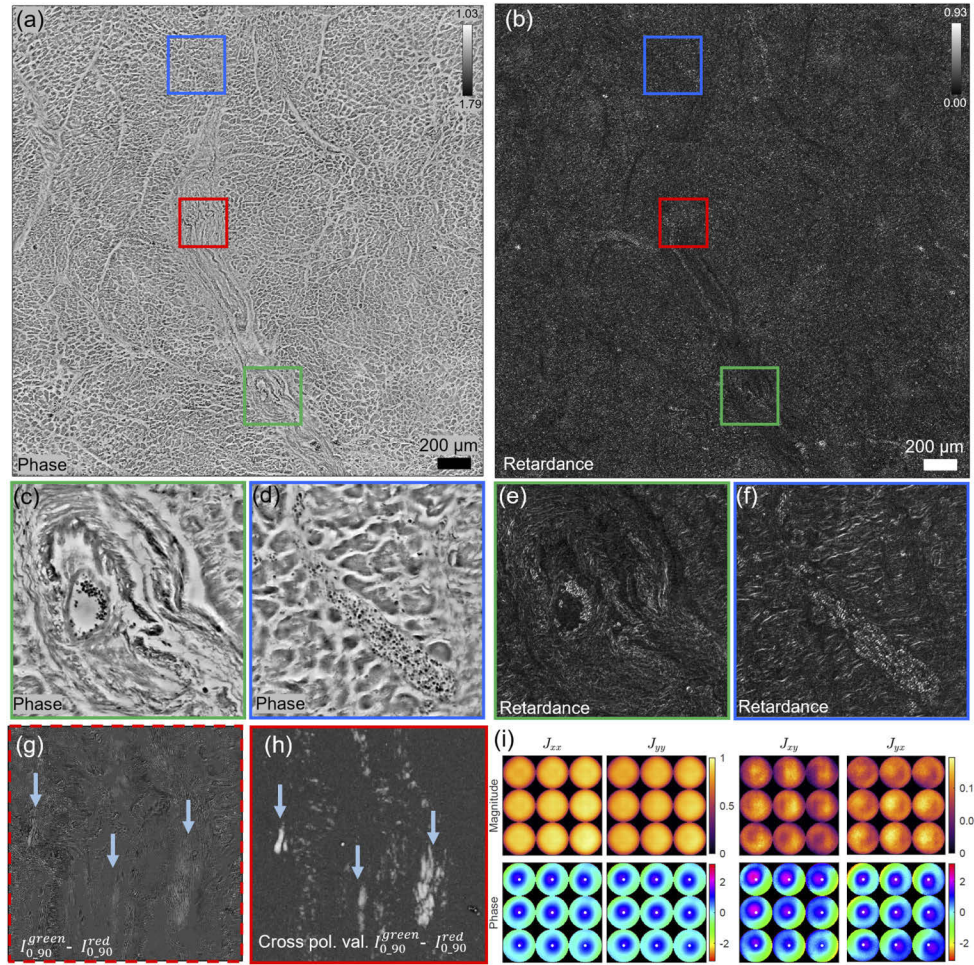


Fig. 5. Large-FOV vFP reconstruction of thin cardiac tissue section stained with Congo red dye. (a) Phase reconstruction. (b) Retardance reconstruction. (c,d) Zoom-ins of (a). (e,f) Zoom-ins of (b). (g) Difference of green and red intensity image under cross-polarization, simulated using the reconstructed sample Jones metrics. (h) Validation via brightfield microscope imaging (NA=0.25) with crossed polarizers, shown as the difference between red and green intensity measurements. (i) Spatially-varying pupils, plotted as the magnitude and phase of the Jones matrix components (at 525 nm). White dots denote the center of the pupil to improve visualization of shifts.

Reconstructing a large FOV with vFP additionally allows us to examine how the recovered Jones matrix of the imaging system pupil function differs between on-axis and off-axis sample positions (Fig. 5(j)). Here, we divided the reconstruction FOV into 3×3 regions and averaged all pupils within each region. The Jones matrix pupil phase patterns experience a shift from the center for off-axis locations [54]. Interestingly, the J_{xy} and J_{yx} pupil amplitudes are spatially varying, unlike J_{xx} and J_{yy} . Higher-NA objectives or cheaper plastic lenses may exhibit stronger polarization effects, which will be the subject of future investigation.

5. Discussion and conclusion

This paper proposes a new computational microscopy method, termed vectorial Fourier ptychography (vFP), to measure the complex amplitude and phase transmission of a thin sample along with its polarization properties contained within its complex Jones matrix. As a synthetic aperture imaging technique, vFP provides a means to obtain high-resolution Jones matrix measurements over a wide FOV without any complex moving parts. Through a simple modification of a conventional polarized light microscope (i.e., replacing the source with an LED array) and a new computational reconstruction algorithm, we demonstrated that our method can jointly recover a vectorial image of complex-valued 2×2 Jones matrices in a variety of calibrated phantoms and biological samples, along with estimation of the 2×2 Jones matrix summarizing the imaging system's vectorial response (i.e., its polarization-dependent aberrations).

As this initial demonstration was a proof of concept, there are several avenues for future direction. To improve acquisition speed, vFP can certainly borrow LED multiplexing [46], multispectral, [55] or multi-aperture [56] strategies previously demonstrated in conventional FP. Furthermore, the approach could also utilize a polarization-sensitive digital image sensor [40,42], which could reduce the amount of required captured data or otherwise improve vFP reconstruction fidelity. In addition, a screen display-based illumination mechanism could be adopted [57] to miniaturize the imaging system. While the present work was restricted to thin samples, additional theoretical development of the vFP framework may allow for 3D polarization microscopy [30,42] in the future. Moreover, additional development may also account for the partial coherence of the LED illumination employed by vFP within the Stokes formalism [42]. Finally, since vFP can jointly estimate and account for the polarization properties of the imaging system, our method could be applied to low-cost microscopes employing plastic lenses, which are known to exhibit birefringence effects under strain. Given the experimental simplicity of our method and the broad range of anisotropic biological samples, vFP could be widely adopted as a significant extension of conventional FP and polarized light microscopy.

Funding. 3M Foundation (Non-tenured Faculty Award); Duke-Coulter Translational Partnership Grant.

Acknowledgments. We would like to thank Dr. Shalin Mehta, Dr. Ian Sigal, Dr. Bin Yang, Dr. Li-Hao Yeh, and Dr. Lars Loetgering for helpful guidance and feedback.

Disclosures. RH: Ramona Optics Inc. (F,I,P,S)

Data availability. Data underlying the results presented in this paper are not publicly available at this time but may be obtained from the authors upon reasonable request.

Supplemental document. See [Supplement 1](#) for supporting content.

References

1. R. A. Chipman, W. S. T. Lam, and G. Young, *Polarized Light and Optical Systems* (CRC press, 2018).
2. M. Wolman, "Polarized light microscopy as a tool of diagnostic pathology," *J. Histochem. Cytochem.* **23**(1), 21–50 (1975).
3. L.-W. Jin, K. A. Claborn, M. Kurimoto, M. A. Geday, I. Maezawa, F. Sohraby, M. Estrada, W. Kaminsky, and B. Kahr, "Imaging linear birefringence and dichroism in cerebral amyloid pathologies," *Proc. Natl. Acad. Sci. U. S. A.* **100**(26), 15294–15298 (2003).
4. B. S. Manjunatha, A. Agrawal, and V. Shah, "Histopathological evaluation of collagen fibers using picosirius red stain and polarizing microscopy in oral squamous cell carcinoma," *J. Can. Res. Ther.* **11**(2), 272 (2015).

5. C. He, H. He, J. Chang, Y. Dong, S. Liu, N. Zeng, Y. He, and H. Ma, "Characterizing microstructures of cancerous tissues using multispectral transformed Mueller matrix polarization parameters," *Biomed. Opt. Express* **6**(8), 2934–2945 (2015).
6. Y. Zhang, S. Y. C. Lee, Y. Zhang, D. Furst, J. Fitzgerald, and A. Ozcan, "Wide-field imaging of birefringent synovial fluid crystals using lens-free polarized microscopy for gout diagnosis," *Sci. Rep.* **6**(1), 1–14 (2016).
7. N.-J. Jan, J. L. Grimm, H. Tran, K. L. Lathrop, G. Wollstein, R. A. Bilonick, H. Ishikawa, L. Kagemann, J. S. Schuman, and I. A. Sigal, "Polarization microscopy for characterizing fiber orientation of ocular tissues," *Biomed. Opt. Express* **6**(12), 4705–4718 (2015).
8. A. H. Badreddine, T. Jordan, and I. J. Bigio, "Real-time imaging of action potentials in nerves using changes in birefringence," *Biomed. Opt. Express* **7**(5), 1966–1973 (2016).
9. C. He, H. He, J. Chang, B. Chen, H. Ma, and M. J. Booth, "Polarisation optics for biomedical and clinical applications: a review," *Light: Sci. Appl.* **10**(1), 194 (2021).
10. M. Koike-Tani, T. Tani, S. B. Mehta, A. Verma, and R. Oldenbourg, "Polarized light microscopy in reproductive and developmental biology," *Mol. Reprod. Dev.* **82**(7-8), 548–562 (2015).
11. N. Panwar and R. Sharma, "A review on influence of mineralogy and diagenesis on spectral induced polarization measurements in carbonate rocks," in *Petro-physics and Rock Physics of Carbonate Reservoirs* (Springer, 2020), pp. 115–125.
12. K. Zhanghao, W. Liu, M. Li, Z. Wu, X. Wang, X. Chen, C. Shan, H. Wang, X. Chen, Q. Dai, P. Xi, and D. Jin, "High-dimensional super-resolution imaging reveals heterogeneity and dynamics of subcellular lipid membranes," *Nat. Commun.* **11**(1), 5890 (2020).
13. J. Lu, H. Mazidi, T. Ding, O. Zhang, and M. D. Lew, "Single-molecule 3D orientation imaging reveals nanoscale compositional heterogeneity in lipid membranes," *Angew. Chem. Int. Ed.* **59**, 17572–17579 (2020).
14. S.-M. Guo, L.-H. Yeh, J. Folkesson, I. E. Ivanov, A. P. Krishnan, M. G. Keefe, E. Hashemi, D. Shin, B. B. Chhun, N. H. Cho, M. D. Leonetti, M. H. Han, T. J. Nowakowski, and S. B. Mehta, "Revealing architectural order with quantitative label-free imaging and deep learning," *eLife* **9**, e55502 (2020).
15. G. Zheng, X. Ou, R. Horstmeyer, J. Chung, and C. Yang, "Fourier ptychographic microscopy: a gigapixel superscope for biomedicine," *Opt. Photonics News* **25**(4), 26–33 (2014).
16. G. Zheng, R. Horstmeyer, and C. Yang, "Wide-field, high-resolution fourier ptychographic microscopy," *Nat. Photonics* **7**(9), 739–745 (2013).
17. S. Song, J. Kim, S. Hur, J. Song, and C. Joo, "Large-area, high-resolution birefringence imaging with polarization-sensitive Fourier ptychographic microscopy," *ACS Photonics* **8**(1), 158–165 (2021).
18. P. Ferrand, A. Baroni, M. Allain, and V. Chamard, "Quantitative imaging of anisotropic material properties with vectorial ptychography," *Opt. Lett.* **43**(4), 763–766 (2018).
19. N.-J. Jan, K. Lathrop, and I. A. Sigal, "Collagen architecture of the posterior pole: high-resolution wide field of view visualization and analysis using polarized light microscopy," *Invest. Ophthalmol. Visual Sci.* **58**(2), 735–744 (2017).
20. A. J. Howie, D. B. Brewer, D. Howell, and A. P. Jones, "Physical basis of colors seen in Congo red-stained amyloid in polarized light," *Lab. Invest.* **88**(3), 232–242 (2008).
21. H. Puchtler, F. Waldrop, and S. Meloan, "A review of light, polarization and fluorescence microscopic methods for amyloid," *Appl. Pathol.* **3**, 5–17 (1985).
22. J. L. Pezzaniti and R. A. Chipman, "Mueller matrix imaging polarimetry," *Opt. Eng.* **34**(6), 1558–1568 (1995).
23. D. H. Goldstein, *Polarized Light* (CRC Press, 2017).
24. A. H. Hielscher, A. A. Eick, J. R. Mourant, D. Shen, J. P. Freyer, and I. J. Bigio, "Diffuse backscattering mueller matrices of highly scattering media," *Opt. Express* **1**(13), 441–453 (1997).
25. G. Yao and L. V. Wang, "Two-dimensional depth-resolved Mueller matrix characterization of biological tissue by optical coherence tomography," *Opt. Lett.* **24**(8), 537–539 (1999).
26. R. C. Jones, "A new calculus for the treatment of optical systems i. description and discussion of the calculus," *J. Opt. Soc. Am.* **31**(7), 488–493 (1941).
27. Z. Wang, L. J. Millet, M. U. Gillette, and G. Popescu, "Jones phase microscopy of transparent and anisotropic samples," *Opt. Lett.* **33**(11), 1270–1272 (2008).
28. S. Aknoun, M. Aurrand-Lions, B. Wattellier, and S. Monneret, "Quantitative retardance imaging by means of quadri-wave lateral shearing interferometry for label-free fiber imaging in tissues," *Opt. Commun.* **422**, 17–27 (2018).
29. Y. Jiao, M. E. Kandel, X. Liu, W. Lu, and G. Popescu, "Real-time Jones phase microscopy for studying transparent and birefringent specimens," *Opt. Express* **28**(23), 34190–34200 (2020).
30. A. Saba, J. Lim, A. B. Ayoub, E. E. Antoine, and D. Psaltis, "Polarization-sensitive optical diffraction tomography," *Optica* **8**(3), 402–408 (2021).
31. T. Colomb, P. Dahlgren, D. Beghuin, E. Cuche, P. Marquet, and C. Depeursinge, "Polarization imaging by use of digital holography," *Appl. Opt.* **41**(1), 27–37 (2002).
32. Y. Kim, J. Jeong, J. Jang, M. W. Kim, and Y. Park, "Polarization holographic microscopy for extracting spatio-temporally resolved Jones matrix," *Opt. Express* **20**(9), 9948–9955 (2012).
33. T. D. Yang, K. Park, Y. G. Kang, K. J. Lee, B.-M. Kim, and Y. Choi, "Single-shot digital holographic microscopy for quantifying a spatially-resolved Jones matrix of biological specimens," *Opt. Express* **24**(25), 29302–29311 (2016).

34. B. Ge, Q. Zhang, R. Zhang, J.-T. Lin, P.-H. Tseng, C.-W. Chang, C.-Y. Dong, R. Zhou, Z. Yaqoob, I. Bischofberger, and P. T. C. So, "Single-shot quantitative polarization imaging of complex birefringent structure dynamics," arXiv preprint arXiv:2106.06118 (2021).
35. J. F. De Boer, C. K. Hitzenberger, and Y. Yasuno, "Polarization sensitive optical coherence tomography—a review," *Biomed. Opt. Express* **8**(3), 1838–1873 (2017).
36. F. Massoumian, R. Juškaitis, M. Neil, and T. Wilson, "Quantitative polarized light microscopy," *J. Microsc.* **209**(1), 13–22 (2003).
37. R. Oldenbourg, "Polarized light microscopy: principles and practice," Cold Spring Harbor Protocols **2013**, pdb-top078600 (2013).
38. S. B. Mehta, M. Shribak, and R. Oldenbourg, "Polarized light imaging of birefringence and diattenuation at high resolution and high sensitivity," *J. Opt.* **15**(9), 094007 (2013).
39. S. Shin, K. Lee, Z. Yaqoob, P. T. So, and Y. Park, "Reference-free polarization-sensitive quantitative phase imaging using single-point optical phase conjugation," *Opt. Express* **26**, 26858–26865 (2018).
40. B. Bai, H. Wang, T. Liu, Y. Rivenson, J. FitzGerald, and A. Ozcan, "Pathological crystal imaging with single-shot computational polarized light microscopy," *J. Biophotonics* **13**, e201960036 (2020).
41. Q. Song, A. Baroni, R. Sawant, P. Ni, V. Brandli, S. Chenot, S. Vézian, B. Damlano, P. de Mierri, S. Khadir, P. Ferrand, and P. Genevet, "Ptychography retrieval of fully polarized holograms from geometric-phase metasurfaces," *Nat. Commun.* **11**(1), 1–8 (2020).
42. L.-H. Yeh, I. E. Ivanov, S.-M. Guo, B. B. Chhun, E. Hashemi, M. H. Han, and S. B. Mehta, "upti: uniaxial permittivity tensor imaging of intrinsic density and anisotropy," in *Novel Techniques in Microscopy* (Optical Society of America, 2021), pp. NM3C–4.
43. R. Horstmeyer and C. Yang, "A phase space model of fourier ptychographic microscopy," *Opt. Express* **22**(1), 338–358 (2014).
44. P. C. Konda, L. Loetgering, K. C. Zhou, S. Xu, A. R. Harvey, and R. Horstmeyer, "Fourier ptychography: current applications and future promises," *Opt. Express* **28**(7), 9603–9630 (2020).
45. X. Ou, G. Zheng, and C. Yang, "Embedded pupil function recovery for Fourier ptychographic microscopy," *Opt. Express* **22**(5), 4960–4972 (2014).
46. L. Tian, X. Li, K. Ramchandran, and L. Waller, "Multiplexed coded illumination for Fourier ptychography with an led array microscope," *Biomed. Opt. Express* **5**(7), 2376–2389 (2014).
47. A. Maiden, D. Johnson, and P. Li, "Further improvements to the ptychographical iterative engine," *Optica* **4**(7), 736–745 (2017).
48. K. Kreutz-Delgado, "The complex gradient operator and the CR-calculus," arXiv preprint arXiv:0906.4835 (2009).
49. X. Ou, R. Horstmeyer, G. Zheng, and C. Yang, "High numerical aperture Fourier ptychography: principle, implementation and characterization," *Opt. Express* **23**(3), 3472–3491 (2015).
50. V. V. Tuchin, "Polarized light interaction with tissues," *J. Biomed. Opt.* **21**(7), 071114 (2016).
51. B. Yang, P.-Y. Lee, Y. Hua, B. Brazile, S. Waxman, F. Ji, Z. Zhu, and I. A. Sigal, "Instant polarized light microscopy for imaging collagen microarchitecture and dynamics," *J. Biophotonics* **14**, e202000326 (2021).
52. X. Ou, R. Horstmeyer, C. Yang, and G. Zheng, "Quantitative phase imaging via fourier ptychographic microscopy," *Opt. Lett.* **38**(22), 4845–4848 (2013).
53. R. Oldenbourg, "Analysis of edge birefringence," *Biophys. J.* **60**(3), 629–641 (1991).
54. J. P. McGuire and R. A. Chipman, "Polarization aberrations. 1. rotationally symmetric optical systems," *Appl. Opt.* **33**(22), 5080–5100 (1994).
55. L. Loetgering, X. Liu, A. C. De Beurs, M. Du, G. Kuijper, K. S. Eikema, and S. Witte, "Tailoring spatial entropy in extreme ultraviolet focused beams for multispectral ptychography," *Optica* **8**(2), 130–138 (2021).
56. P. C. Konda, J. M. Taylor, and A. R. Harvey, "Multi-aperture Fourier ptychographic microscopy, theory and validation," *Opt. Lasers Eng.* **138**, 106410 (2021).
57. K. C. Lee, K. Lee, J. Jung, S. H. Lee, D. Kim, and S. A. Lee, "A smartphone-based Fourier ptychographic microscope using the display screen for illumination," *ACS Photonics* **8**(5), 1307–1315 (2021).